Università degli Studi di Napoli "Federico II"

SCUOLA POLITECNICA E DELLE SCIENZE DI BASE

DIPARTIMENTO DI INGEGNERIA INDUSTRIALE

CORSO DI LAUREA IN INGEGNERIA AEROSPAZIALE

CLASSE DELLE LAUREE IN INGEGNERIA INDUSTRIALE (L-9)

Elaborato di laurea in Meccanica del Volo

Geometric modelling, stability and control analysis of the unmanned aerial vehicle Elbit Hermes 900 with OpenVSP

Relatore:
Prof. Danilo Ciliberti

Candidato:
Francesco Luongo
Matr. N35003413

ANNO ACCADEMICO 2023 – 2024

A Mamma, Papà, Valeria e Marta.

Abstract

This thesis focuses on the geometric modeling and analysis of the Israeli unmanned aerial vehicle (UAV) Elbit Hermes 900, using the open-source platform OpenVSP. OpenVSP is a parametric tool that allows for the creation of 3D aircraft models, serving as a foundation for subsequent engineering analyses. The stability and control properties of the Hermes 900 have been evaluated using the VSPAERO tool, a fast and reliable solver based on the Vortex Lattice Method (VLM), which is particularly effective for early-stage aircraft design. VLM models the UAV's lifting surfaces as infinitely thin sheets of discrete vortices. By carefully setting up the simulation and refining the geometric model, the analysis provided accurate and meaningful insights into the UAV's stability and control characteristics. The results were compiled and analyzed, offering a comprehensive overview of the Hermes 900's stability and control. While VSPAERO has certain limitations with more complex models, it has proven to be an efficient and practical solution for this study, facilitating rapid and effective preliminary analysis.

Sommario

Questa tesi si concentra sulla modellazione geometrica e l'analisi del velivolo senza pilota (UAV) israeliano Elbit Hermes 900, utilizzando la piattaforma open-source OpenVSP. OpenVSP è uno strumento parametrico che consente la creazione di modelli 3D di velivoli, fungendo da base per successive analisi ingegneristiche. Le proprietà di stabilità e controllo dell'Hermes 900 sono state valutate utilizzando VSPAERO, un solutore veloce e affidabile basato sul Vortex Lattice Method (VLM), particolarmente efficace nelle fasi iniziali della progettazione aeronautica. Il VLM modella le superfici portanti dell'UAV come fogli infinitamente sottili di vortici discreti. Impostando accuratamente la simulazione e affinando il modello geometrico, l'analisi ha fornito informazioni precise e significative sulle caratteristiche di stabilità e controllo dell'UAV. I risultati sono stati raccolti e analizzati, offrendo una panoramica completa della stabilità e del controllo dell'Hermes 900. Sebbene VSPAERO presenti alcune limitazioni con modelli più complessi, si è dimostrato una soluzione efficiente e pratica per questo studio, facilitando un'analisi preliminare rapida ed efficace.

Table of contents

List of figures

List of tables

1. Introduction

1.1 Objectives

The objective of this work is to fully examine the stability and control characteristics of the unmanned aerial vehicle Elbit Hermes 900. This study delivers preliminary data on the UAV's aerodynamic performance, stability, and control, recognizing that both VSPAERO and the Vortex Lattice Method (VLM) have inherent limitations. Additionally, the thesis aims to elucidate the VLM numerical method, including its fundamental theory and its application within the VSPAERO software. The analysis focuses on generating characteristic curves and other essential data for the Hermes 900, such as lift, aerodynamic efficiency, moment coefficient, and drag polar curves for the isolated wing, partial, and complete aircraft configurations. These data are processed using Microsoft Excel to present a detailed overview of the UAV's aerodynamic and stability characteristics. Furthermore, stability observations are conducted by analyzing the UAV's performance at various angles of attack, providing insights into its control behavior under different conditions.

1.2 Layout of work

Chapter 1: In this chapter there will be a brief introduction of the aircraft and its major features.

Chapter 2: This chapter will discuss the vortex lattice method, its assumptions and its basic working.

Chapter 3: This chapter focuses on the 3D modeling process in OpenVSP.

Chapter 4: This chapter discusses the longitudinal stability analysis performed in VSPAERO and its implications.

Chapter 5: This chapter discusses the lateral-directional stability analysis performed in VSPAERO and its implications.

Chapter 6: Conclusions chapter.

1.3 Elbit Hermes 900: characteristics and operational uses

Since the 1970s, Israel has specialized in the design of unmanned aerial vehicles (UAVs) for surveillance and reconnaissance missions. Over time, this expertise has become a significant technological asset, with Israeli military drones now recognized worldwide. Elbit Systems has built a strong reputation in this field due to its exceptional achievements and competitive pricing, with its drones compete with the best American and European models on international markets. One of the most notable successes is the MALE (Medium Altitude Long Endurance) drone, the Hermes 900.

Also known as "Kochav" (which means "star" in Hebrew), this UAV exemplifies Israel's innovative approach to drone design. Developed from the success of its predecessor, the Hermes 450, the Hermes 900 is engineered for medium-altitude, long-endurance missions, capable of flying for over 30 hours and reaching altitudes of up to 9,100 meters. This UAV is equipped to carry a payload of 300 kilograms, including advanced electro-optical sensors, synthetic aperture radar, hyperspectral sensors, and devices for communication and electronic warfare. Built with a combination of metal, light alloys, and composite materials, the Hermes 900 features a straight-wing monoplane design with retractable tricycle landing gear and a distinctive V-tail. Powered by a four-cylinder, turbocharged Rotax Type 914 engine, it operates with such efficiency that it remains almost imperceptible from the ground when cruising at altitude.

Figure 1.1 The Elbit Hermes 900

The Israeli Ministry of Defense quickly adopted the Hermes 900, purchasing thirty units in 2010. These drones proved to be extremely effective in monitoring operations. During the summer of 2014's civil war, when Israeli air and ground forces clashed with Islamic fighters and civilian populations in Gaza, the Elbit Kochav was deployed for the first time in military operations, even though it was still in the testing phase, to track enemy leaders and coordinate airstrikes. Its ability to remain at medium altitude before, during, and after incursions allowed for real-time reporting on the success or failure of operations. Following the conflict, the Hermes 900 continued its testing phase to further refine its capabilities. On November 11, 2015, it was officially introduced into the Israeli Air Force's operational fleet, solidifying its position as a key asset in Israel's military and surveillance operations. The success of the Hermes 900 has not been limited to Israel. This drone has been sold for military use to countries such as Azerbaijan, Brazil, Chile, Colombia, the Philippines, and Switzerland. The Mexican federal police use it against cocaine trafficking, while the European Maritime Safety Agency leased two units to monitor North Atlantic shipping routes. In Brazil, the Hermes 900 is employed for Amazon surveillance and border security [6].

1.3.1 UAV flight stability and control

Stability in a UAV refers to its ability to return to a state of equilibrium after being disturbed during flight, often due to gusts or control inputs. Static stability is the initial response of the aircraft to regain equilibrium upon a disturbance. Dynamic stability, on the other hand, refers to how the aircraft’s response evolves over time. Even with inherent positive static stability, an aircraft might overshoot its equilibrium condition, resulting in oscillations. If these oscillations diminish over time, the aircraft demonstrates positive dynamic stability. Short-lived oscillations indicate high damping, while longer-lasting ones suggest light damping.

The neutral point (NP) is the center of gravity (CG) position where the aircraft achieves neutral static longitudinal stability. Placing the CG forward of the NP results in positive static stability, whereas positioning it aft of the NP leads to static instability. This is quantified by the static margin (SM), which is a non-dimensional measure of the aircraft’s stability. A large SM indicates a highly stable but less maneuverable UAV, while those with a small positive SM are more maneuverable.

During flight, a UAV experiences moments generated by the aerodynamic load distribution and the thrust force not acting through the CG. These aerodynamic moments are represented

by dimensionless coefficients: pitching moment (Cm), rolling moment (Cℓ), and yawing moment (Cn). The values of these coefficients depend on the angle of attack (α), Reynolds number (Re), Mach number (M) and sideslip angle (β).

For a UAV to have longitudinal static stability, the slope of the pitching moment curve must be negative at the equilibrium point. Additionally, to achieve trim at a positive angle of attack (α) and generate effective lift, the Cm at α = 0° should be greater than zero. For lateral static stability, the slope should be negative, while for directional static stability, it must be positive.

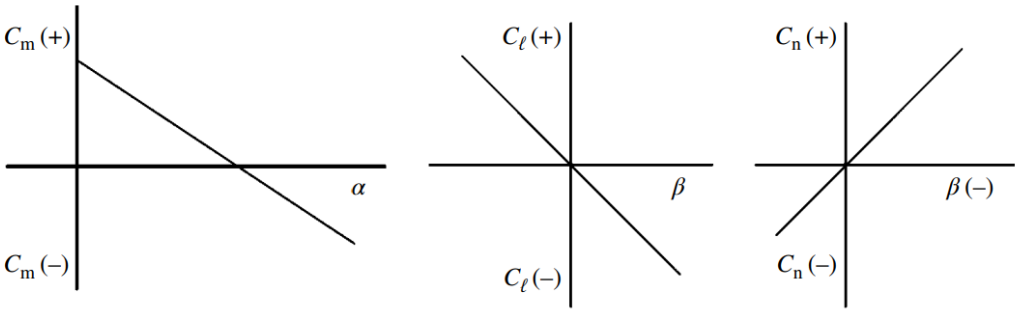

Figure 1.2 Stability conditions in pitch, roll and yaw

2. Vortex Lattice Method

The Vortex Lattice Method (VLM) is a numerical method used in computational fluid dynamics that allows the analysis of flow around wings with finite span. The VLM represents lifting surfaces, such as a wing, as an infinitely thin sheet of discrete vortices. The method enables the calculation of the velocity field around the wing with a relatively low computational load, allowing for the determination of pressure distribution and induced drag. Consequently, aerodynamic coefficients and stability derivatives can be derived. This information is particularly useful in the early stages of design, where little is known about the wing's characteristics, and a quick and accurate evaluation of the load acting on the structure is needed to begin the sizing process.

2.1 Theory

2.1.1 Assumptions

The method is based on the following assumptions:

- The flow is incompressible, inviscid, and irrotational.
- The lifting surface is considered thin, so the effect of thickness on aerodynamic forces is neglected.
- The angle of attack and sideslip are assumed to be small.

2.1.2 Flow description

Starting from the hypothesis of irrotational flow, it follows that the vorticity at every point in the flow is zero:

$$\xi = \nabla \times V = 0 \tag{2.1}$$

By introducing φ as a scalar function, we have:

$$\nabla \times (\nabla \varphi) = 0 \tag{2.2}$$

Combining (2.1) and (2.2):

$$V = \nabla\varphi \tag{2.3}$$

This shows that in irrotational flow, the velocity field can be described by the gradient of a scalar function φ, therefore the term velocity potential.

From the mass conservation principle for an incompressible flow:

$$\nabla \cdot V = 0 \tag{2.4}$$

Using the definition of the velocity potential and integrating (2.3) and (2.4):

$$\nabla \cdot (\nabla\varphi) = 0 \tag{2.5}$$

Or equivalently:

$$\nabla^2\varphi = 0 \tag{2.6}$$

The (2.6) equation is the Prandtl-Glauert equation, which describes irrotational and incompressible flow. Thus, a complex flow model under these conditions can be synthesized by summing a series of elementary flows that are also irrotational and incompressible. The VLM is based on these line vortices, as previously mentioned.

2.1.3 Boundary conditions

The Vortex Lattice Method (VLM) utilizes the thin airfoil boundary condition, enabling the linearization of pressure coefficients and simplifying the analysis by allowing the effects of thickness and viscosity to be neglected. Additionally, for symmetric airfoils, the camber effects can also be neglected. This method's strength lies in its ability to simplify complex aerodynamic problems by applying boundary conditions on a flat surface, which can be deflected at an angle of attack, α.

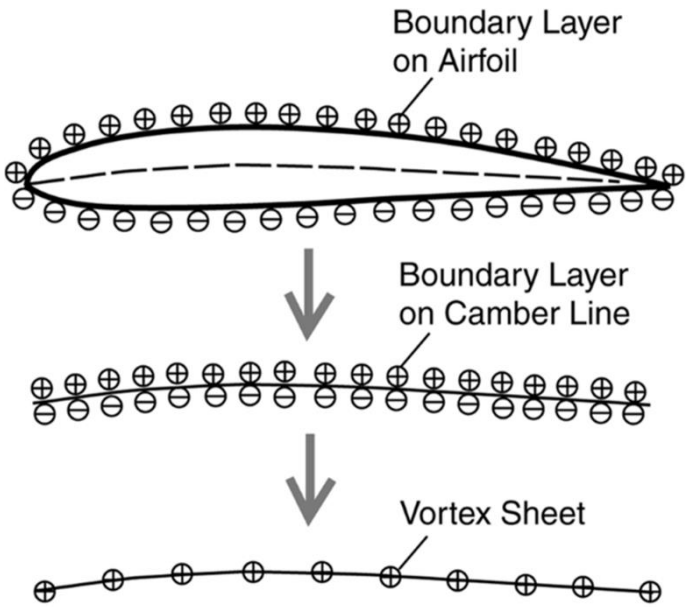

Figure 2.1 Idealization from a boundary layer to a vortex sheet

The core principle of VLM is to ensure that the normal flow across the wing's solid surface remains zero. Mathematically, this boundary condition is expressed as:

$$\nabla(\varphi + \varphi_\infty) = 0 \tag{2.7}$$

This implies that the sum of the normal velocity components induced by the wing's bound vortices w_b , the wake w_i , and the free-stream velocity V_∞ must equal zero:

$$w_b + w_i + V_\infty \cdot \alpha = 0 \tag{2.8}$$

2.1.4 Biot-Savart law and horseshoe vortex

One of the possible solutions to Laplace's equation is the line vortex. These vortices induce an increment of velocity dV_p at a point P given by the Biot-Savart law:

$$dV_p = \frac{\Gamma}{4\pi} \cdot \frac{dl \times r_{pq}}{|r_{pq}|^3} \tag{2.9}$$

The induced velocity dV_p at a point P, due to a segment of a vortex filament dl at a point q, is directly proportional to the vortex strength Γ (which has the same sign as the vorticity, positive if clockwise) and inversely proportional to the square of the distance between dl and P, r_{pq}.

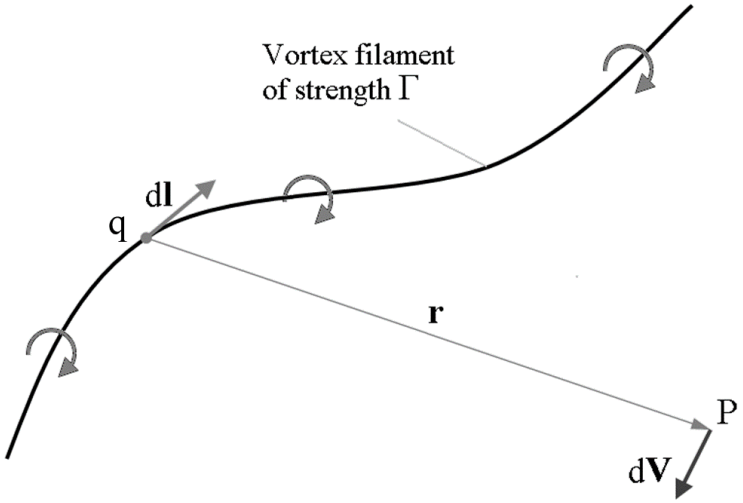

Figure 2.2 Velocity induced by a vortex filament

The VLM uses a specific type of vortex and is an extension of Prandtl lifting line theory, where the wing of an aircraft is modelled as an infinite number of horseshoe vortices rather than just one per wing. Each horseshoe vortex consists of four segments: two trailing vortex segments (ab and cd) aligned parallel to the free stream and extending to infinity, and two finite segments (bc and ad). Typically, the effects of segment ad are ignored due to its infinite distance, reducing the horseshoe vortex to three effective parts. The lifting properties of the wing are represented by the bound vortex segment (bc), while the wake is modeled by the two trailing vortex lines. According to the Biot-Savart law, the induced velocity at a point P can be generally expressed as:

$$V_p = V_{bc} + V_{b\infty} + V_{c\infty} \tag{2.10}$$

To accurately evaluate V_p , it is essential to establish the locations of the vortex and the control point P, typically positioned at the ¼ chord and ¾ chord points, respectively (a practice known as the "¼-¾ rule"). However, this is not a theoretical law but rather a convention that works well and has become standard practice. This placement ensures that the induced velocity at the control point matches the velocity at the boundary according to the surface boundary condition.

In the VLM, the wing's surface is divided into a finite number of panels (both chordwise and spanwise), with each panel containing a horseshoe vortex. Each vortex has its own circulation and induces a velocity at its control point. Circulation is a key concept, as it relates to the lift generated by the wing, according to the Kutta-Joukowski theorem. In the VLM, by

determining the circulation for each horseshoe vortex, the total lift can be calculated by summing the contributions from all the panels. Thus, the circulation not only characterizes the strength of each vortex but also directly determines the aerodynamic lift that the wing produces.

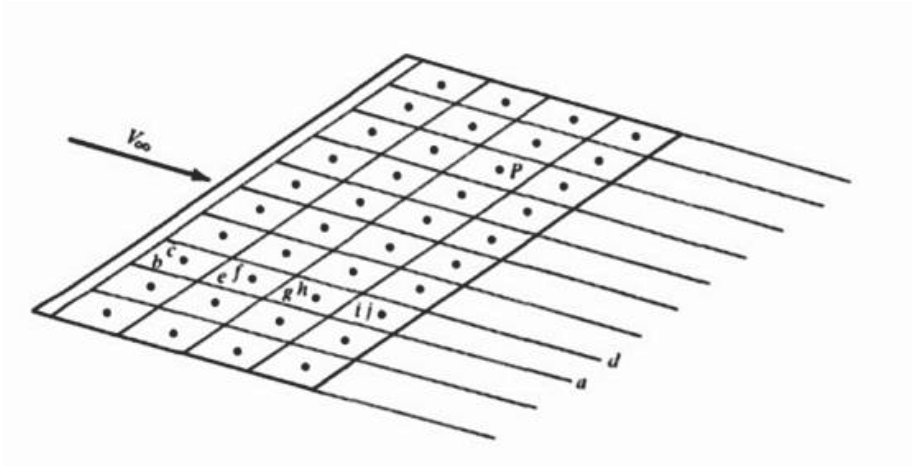

Figure 2.3 Horseshoe vortex lattice

2.2 VSPAERO

In practice, VSPAERO does not strictly use the Vortex Lattice Method (VLM); instead, it employs a mean surface technique. This approach accounts for the camber effects of wings and fuselages while ignoring thickness. In this method, wings are modeled with the same camber as the selected airfoil, while fuselages are represented by two intersecting mean surfaces arranged in a cross shape. As a ring vortex-based solver, VSPAERO uses a finite number of ring vortices with varying intensities on the wing surface.

It is important to note that at this level of analysis, viscous drag cannot be evaluated, but induced drag can be computed based on lift production. Since the VLM relies on potential flow theory, its applicability is limited to the linear aerodynamic region, specifically within the low angle of attack flight domain.

3. Geometric Modelling

3.1 OpenVSP

OpenVSP (Open Vehicle Sketch Pad) is an open-source tool designed for parametric aircraft geometry, initially developed by NASA. It allows users to construct 3D aircraft models using standard engineering parameters and offers a range of integrated tools for conducting structural and aerodynamic analyses. These models can be easily exported into formats tailored for further engineering evaluation.

When OpenVSP starts up, a large working window appears alongside a Geometry Browser. The Geometry Browser lists all the individual components of the aircraft model, allowing the user to add and manage each element. Selecting a component opens its geometry window, where the user can adjust its parameters to refine the design.

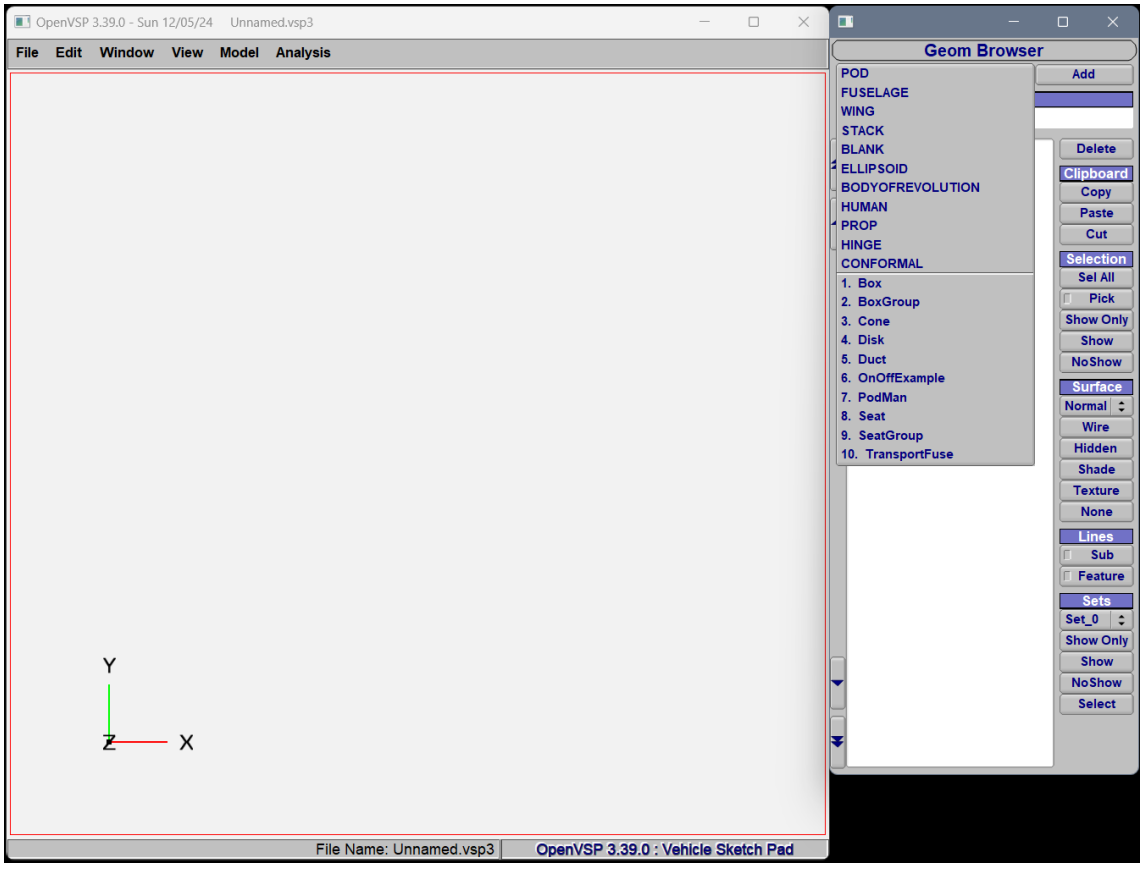

Figure 3.1 OpenVSP workspace and geometry browser with all predefined geometries

3.2 Elbit Hermes 900 modelling process

3.2.1 References

The model's dimensions were derived from manuals, photographs, and reference images, such as the one in the Figure 3.2. For measurements that were not directly available, the Adobe Acrobat Reader tool was used to deduce them.

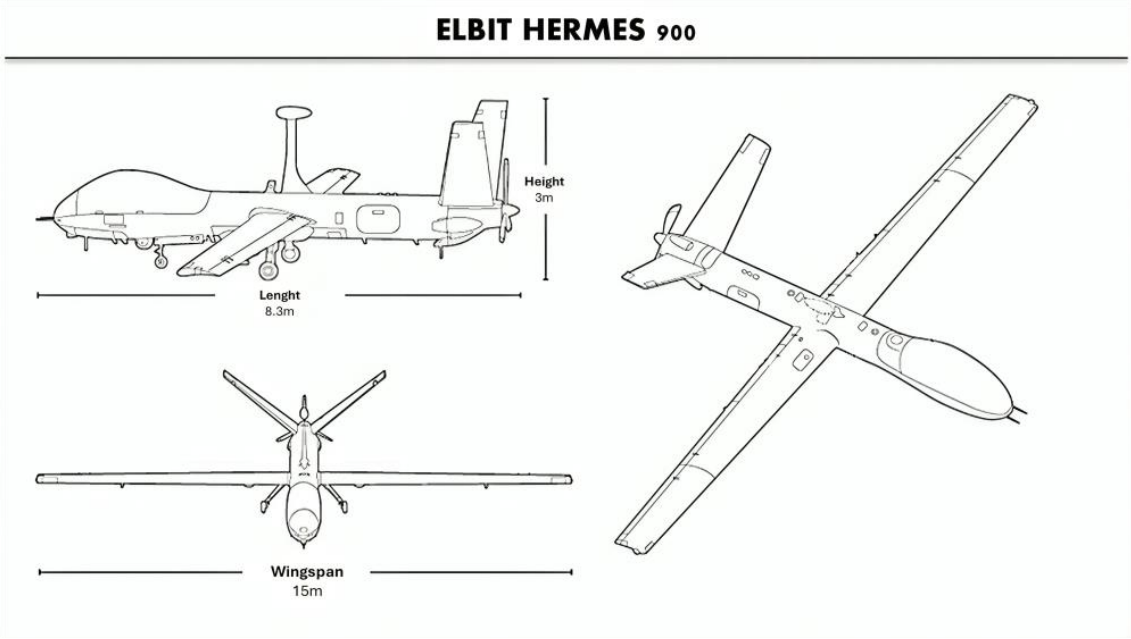

Figure 3.2 Elbit Hermes 900 reference

3.2.2 Wing

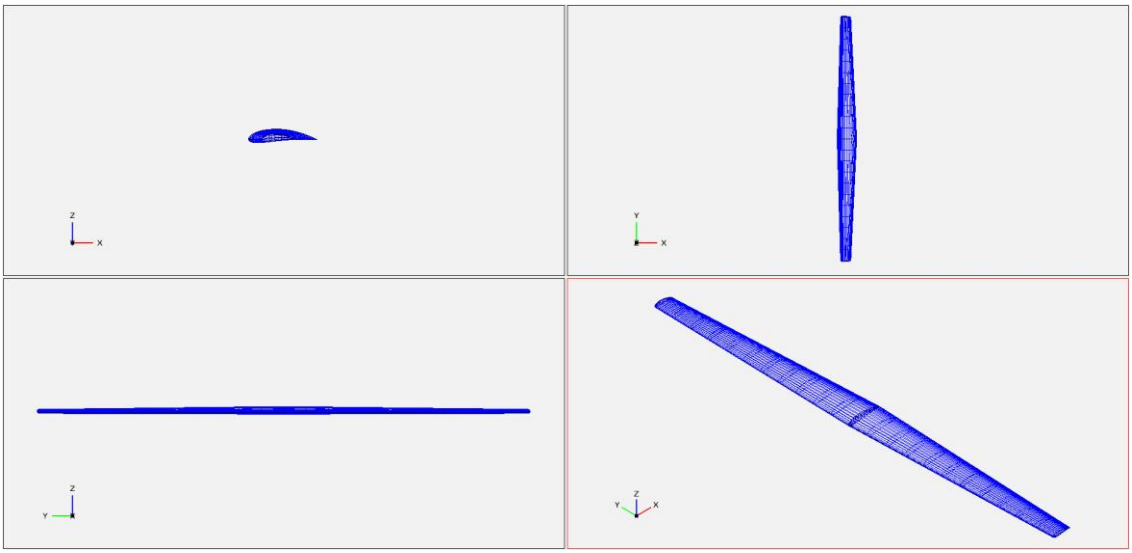

Figure 3.3 The four-view wing

Starting from the most crucial part of any aircraft, the wing. By selecting it from the geometry browser shown above, Figure 3.4 shows all the parameters needed to configure the wing.

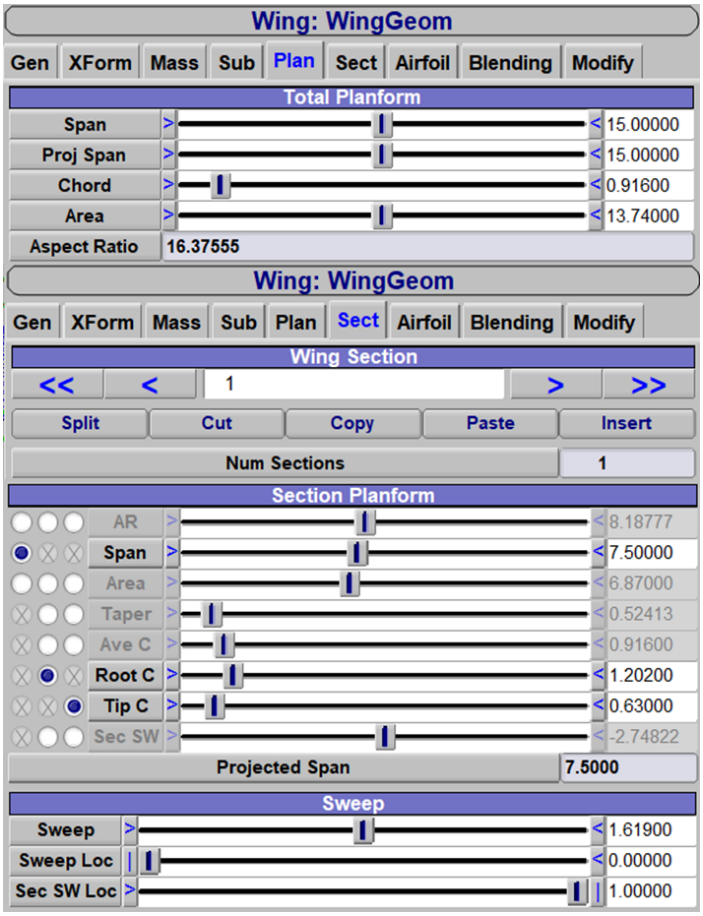

Figure 3.4 Wing parameters

The exact airfoil is not known, but the GOE 228 (MVA H.38) is the closest match. Its parameters and performance data have been sourced from the website www.airfoiltools.com.

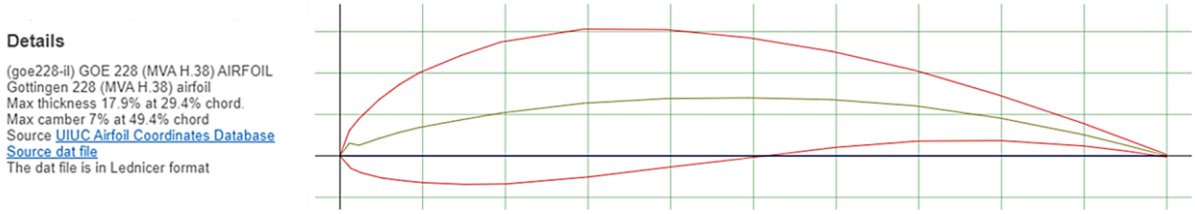

Figure 3.5 Airfoil GOE 228 (MVA H.38) taken from www.airfoiltools.com

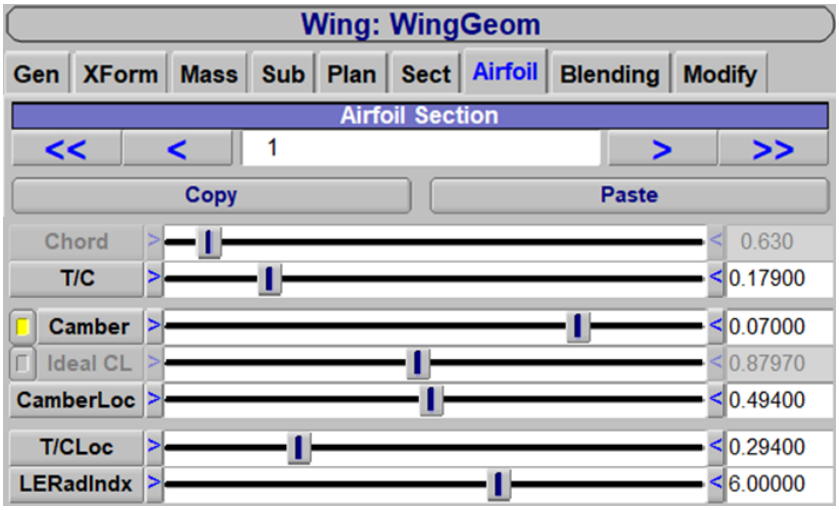

Figure 3.6 Airfoil parameters in OpenVSP

3.2.3 Wing grid adjustments

Once the wing has been introduced, the next step is to refine its grid by adjusting both the chordwise and spanwise directions. The goal in each case is to determine values for W and U that lead the polar curves, generated by varying one parameter while keeping the other constant, to approach an asymptotic behavior at a fixed angle of attack. The initial task involves adjusting the grid in the chordwise direction by modifying the W value using the tools provided in the wing geometry tab. For this evaluation, the U value is set to the default of 16, with the angle of attack fixed at 0°.

W	C_L	$C_{D_{tot}}$	C_{M_y}
21	0.6796	0.0185	-0.0819
37	0.7234	0.0201	-0.0866
53	0.7402	0.0207	-0.0882
77	0.7527	0.0212	-0.0892
101	0.7590	0.0214	-0.0897

Table 3.1 Variations of the aerodynamic coefficients with the W parameter at $\alpha = 0°$

The data reported in Table 3.1 have been plotted in Figure 3.7.

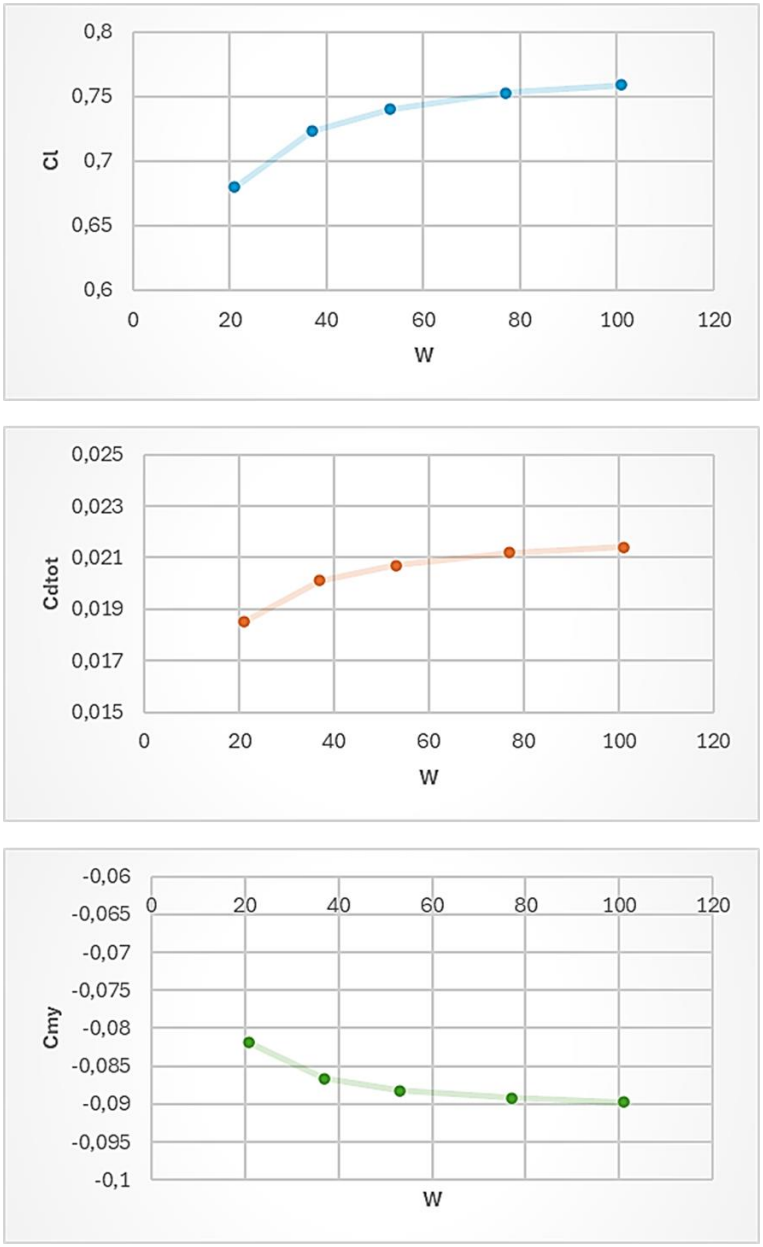

Figure 3.7 Variations of the aerodynamic coefficients with the W parameter at α = 0°

It can be seen from the table and graphs that a suitable value is W = 77.

Building on the previous step, the refinement in the transverse direction was achieved by adjusting the U parameter in the wing geometry window's Sect Tab, while keeping the previously determined W value fixed. It is important to note that increasing the U parameter significantly impacts the solution time, leading to a higher computational cost.

U	C_L	$C_{D_{tot}}$	C_{M_y}
10	0.7535	0.0211	-0.0890
20	0.7508	0.0214	-0.0896
40	0.7490	0.0216	-0.0898
60	0.7491	0.0217	-0.0903

Table 3.2 Variations of the aerodynamic coefficients with the U parameter at α = 0°

The data reported in Table 3.2 have been plotted in Figure 3.8.

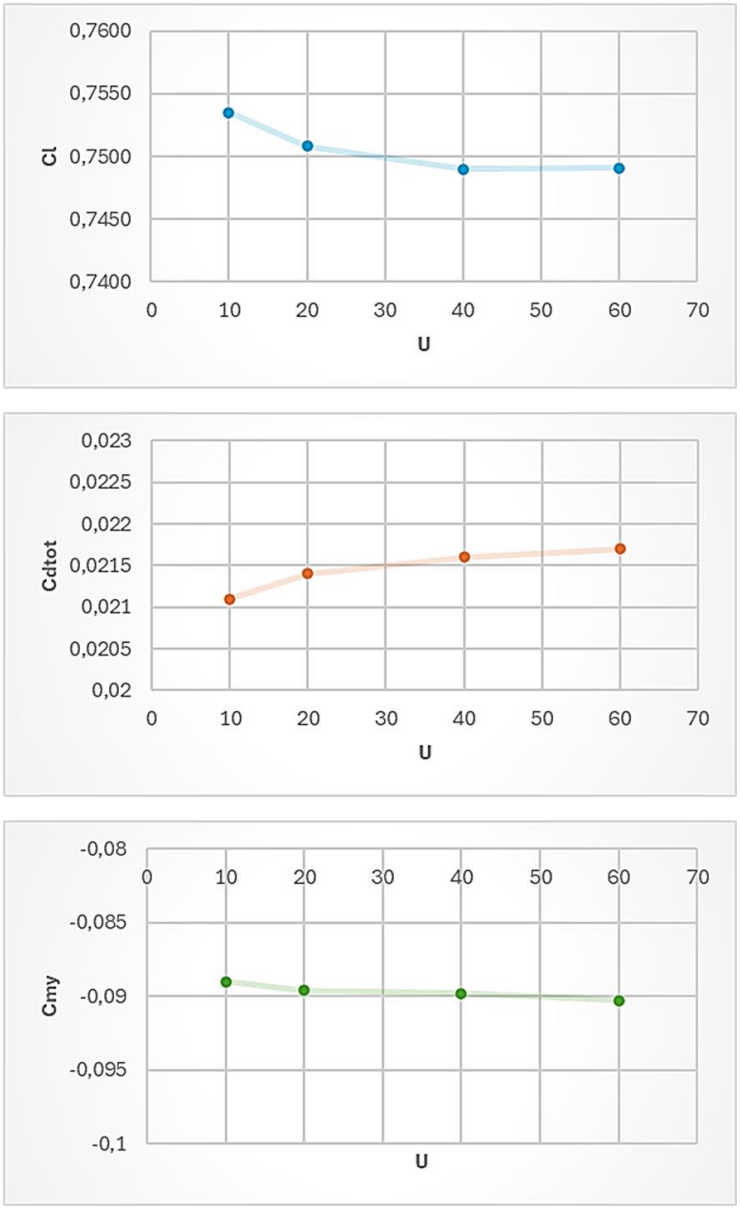

Figure 3.8 Variations of the aerodynamic coefficients with the U parameter at α = 0°

In this case the best value is U = 40. Ultimately, the best values of W and U, i.e. the ones used, are 77 and 40 respectively. The same values will be used on the tailplane.

3.2.4 Fuselage

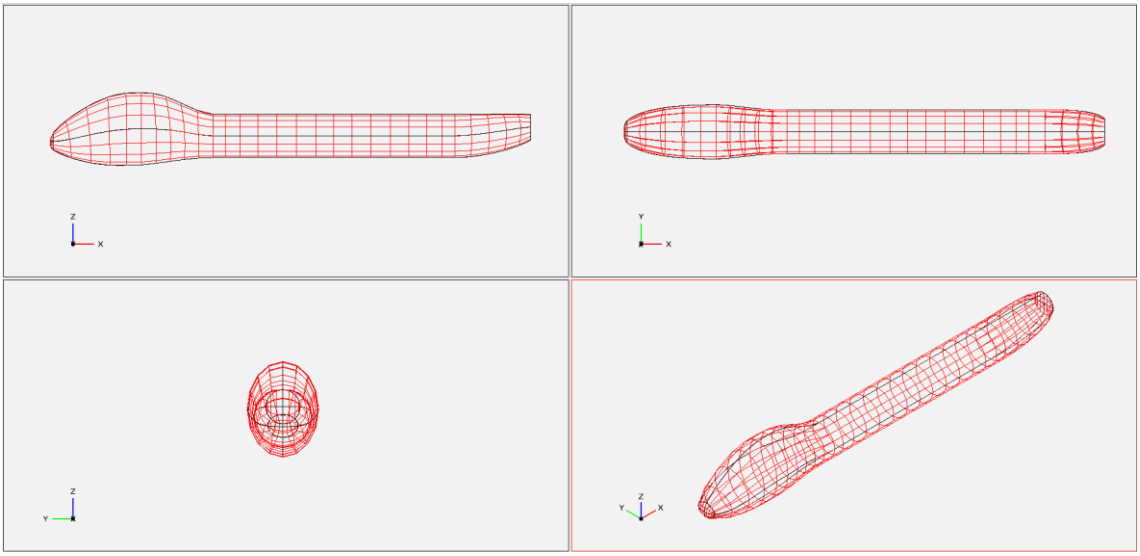

Figure 3.9 The four-view fuselage

The fuselage stands out as the most intricate part of this UAV, largely because of the "dome" located at the front. To accurately model it in OpenVSP, additional sections needed to be inserted. Figure 3.10 shows the parameters used.

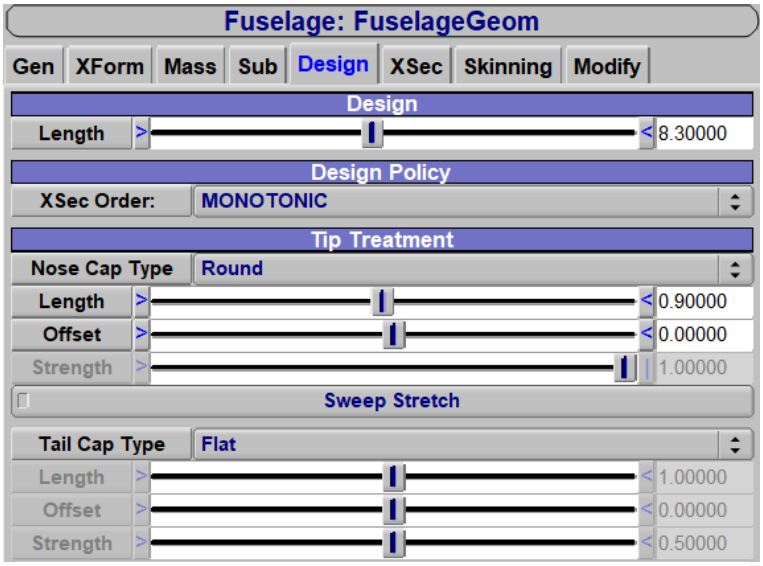

Figure 3.10 Fuselage general parameters

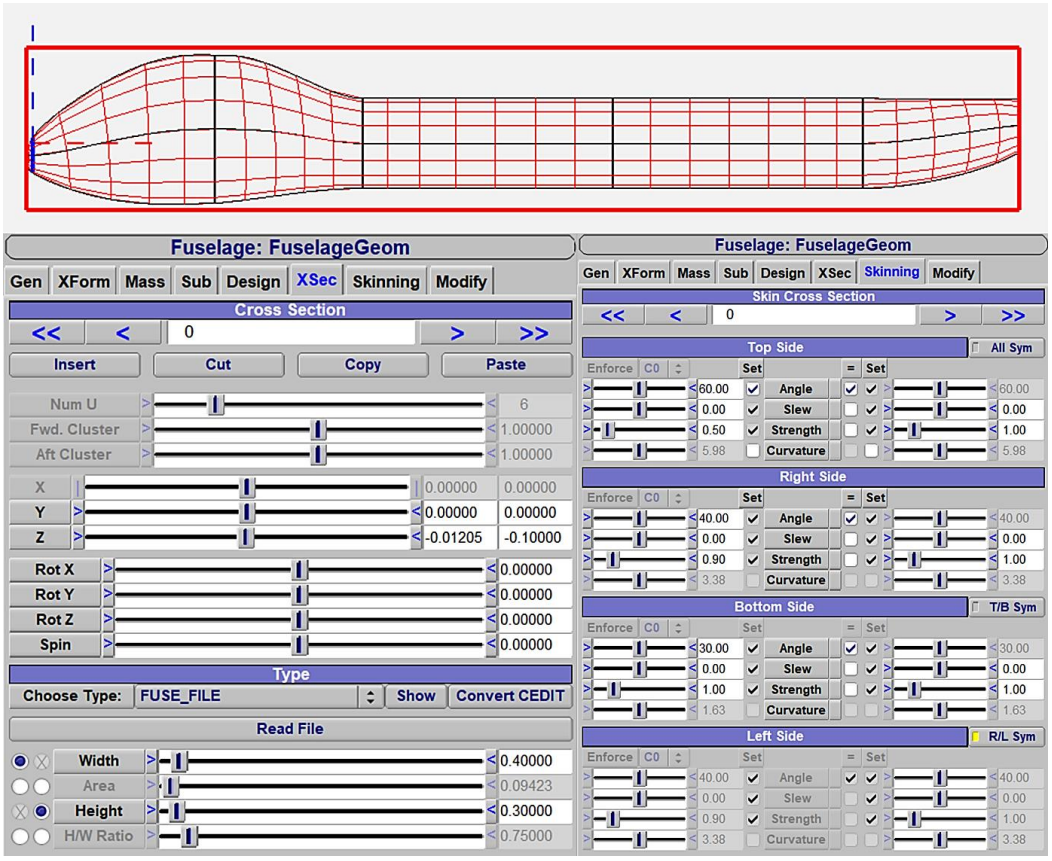

Figure 3.11 Section 0 (nose) parameters

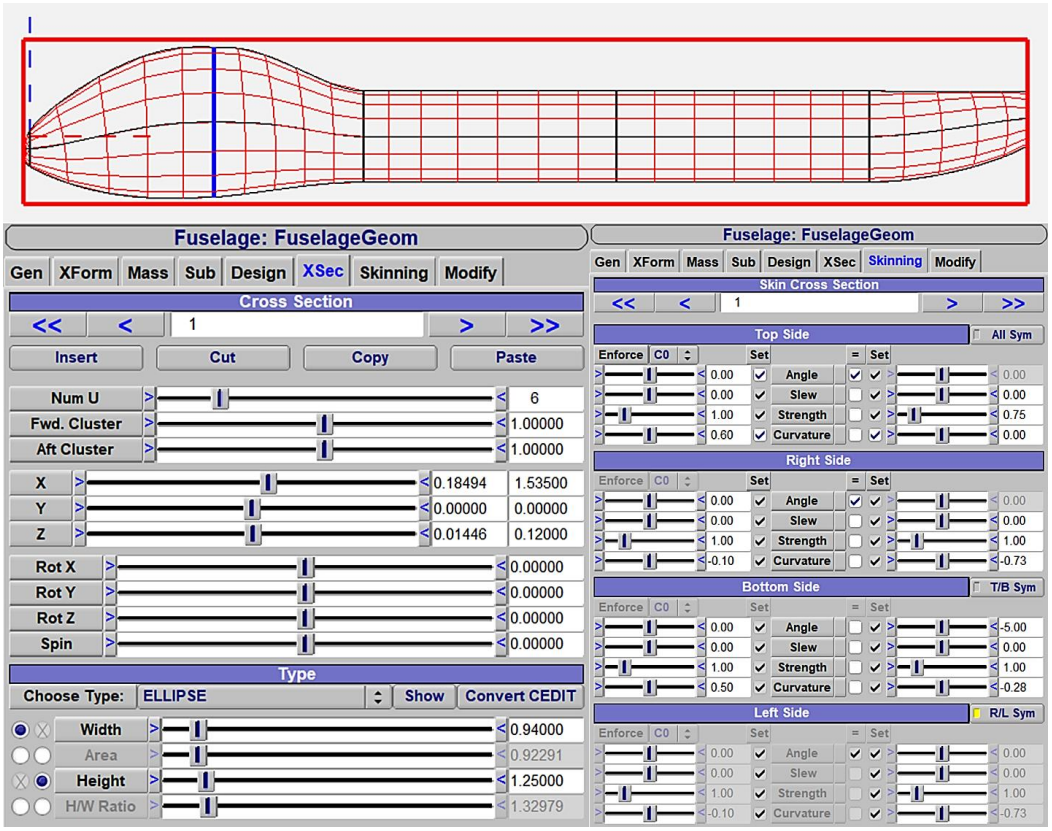

Figure 3.12 Section 1 parameters

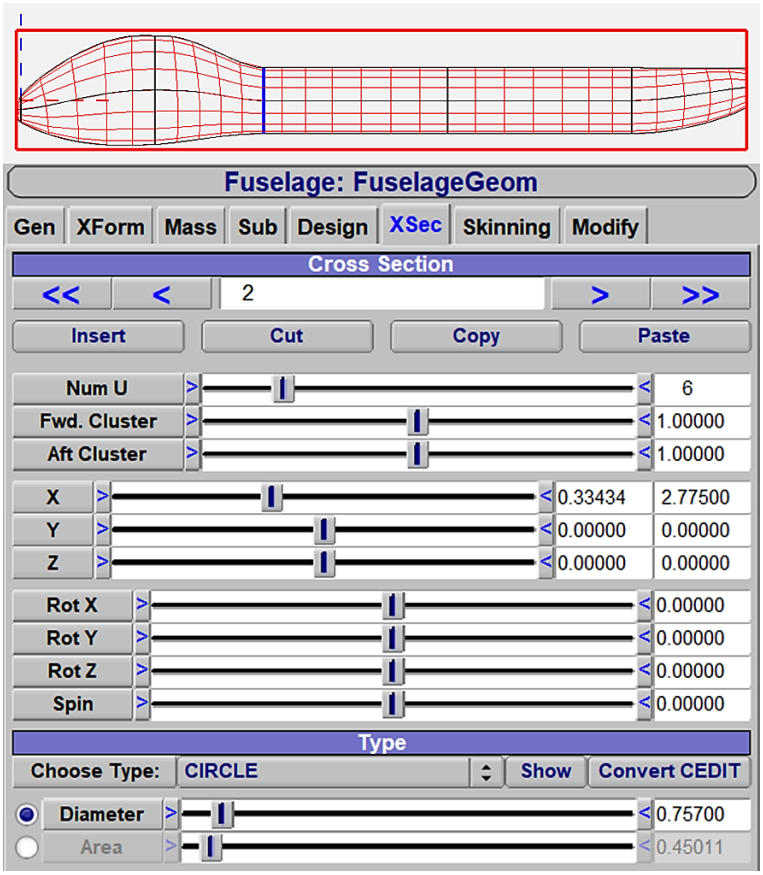

Figure 3.13 Section 2 parameters (same for sections 3 and 4)

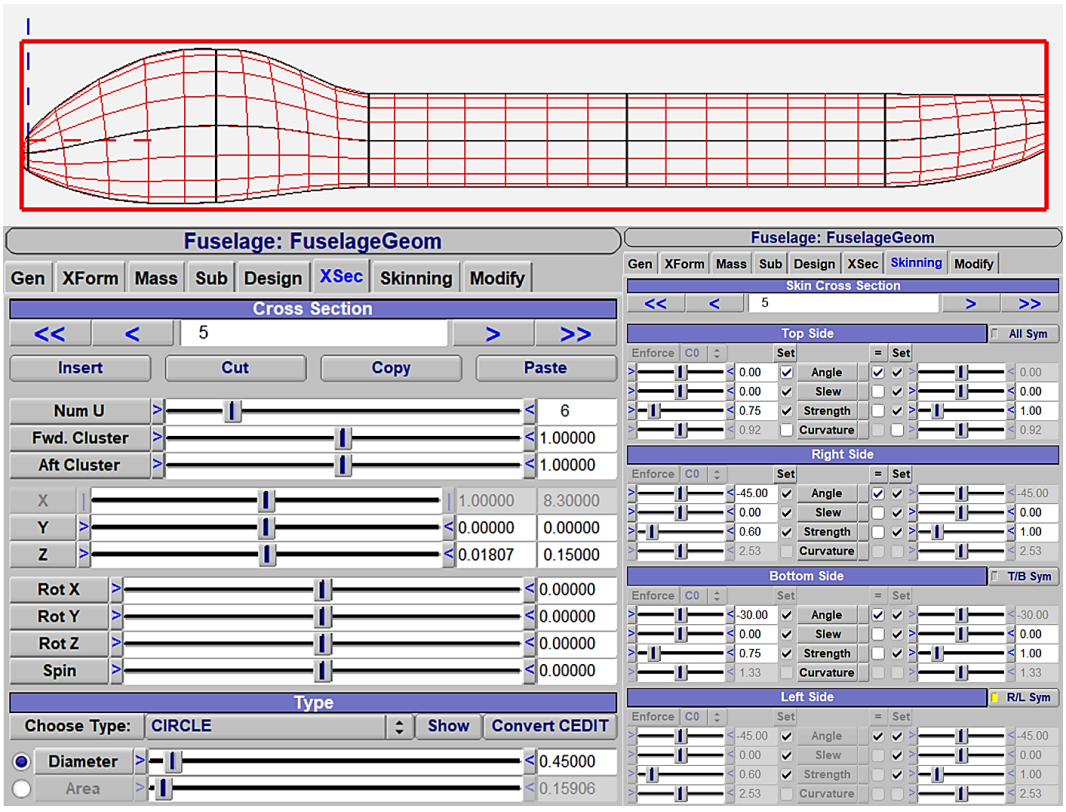

Figure 3.14 Section 5 (tail) parameters

3.2.5 Tailplane

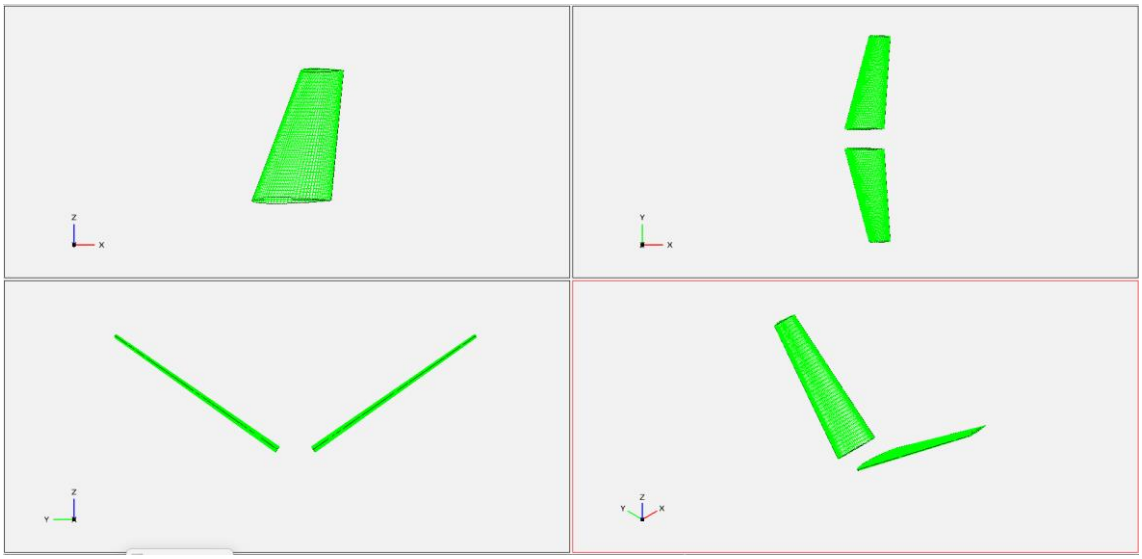

Figure 3.15 The four-view tailplane

The ruddervators are designed as two separate wings with identical parameters. The left ruddervator is a mirrored copy of the right wing, shifted to maintain symmetry. Being fully movable control surfaces, they are modeled as two distinct parts to allow for both symmetrical and independent deflections.

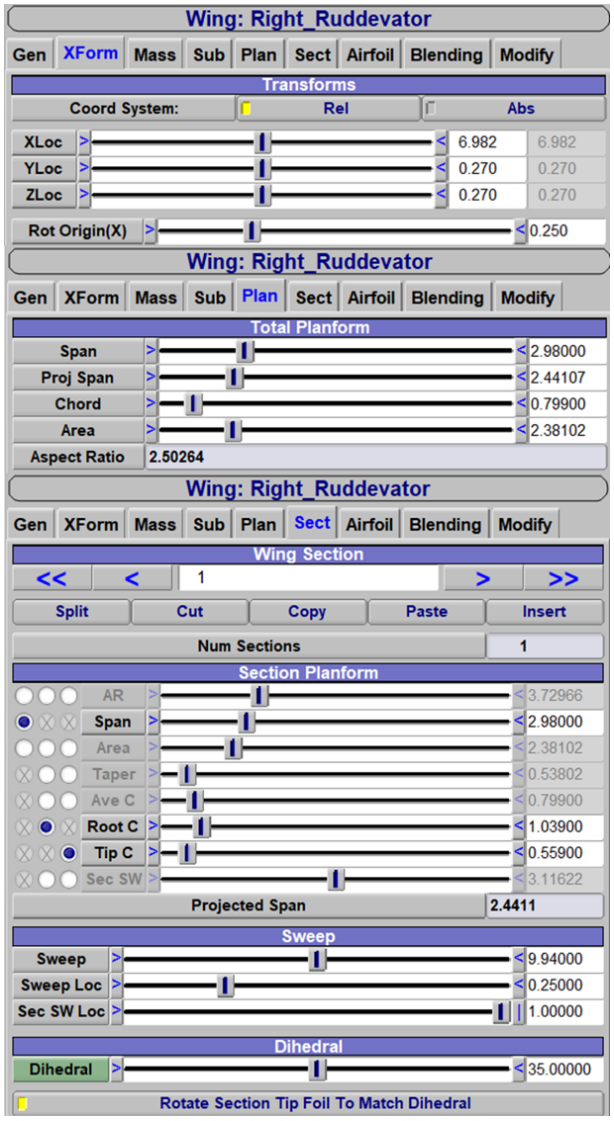

Figure 3.16 Ruddervators parameters

To enable both symmetrical and asymmetrical deflections, two user parameters were set up, connected to the rotation of blank components placed at 25% of the root chord of each ruddervator, where they are attached. The custom UserParms simultaneously rotates the ruddervators around the global Y and Z axes using the cosine and sine of the tail dihedral angle.

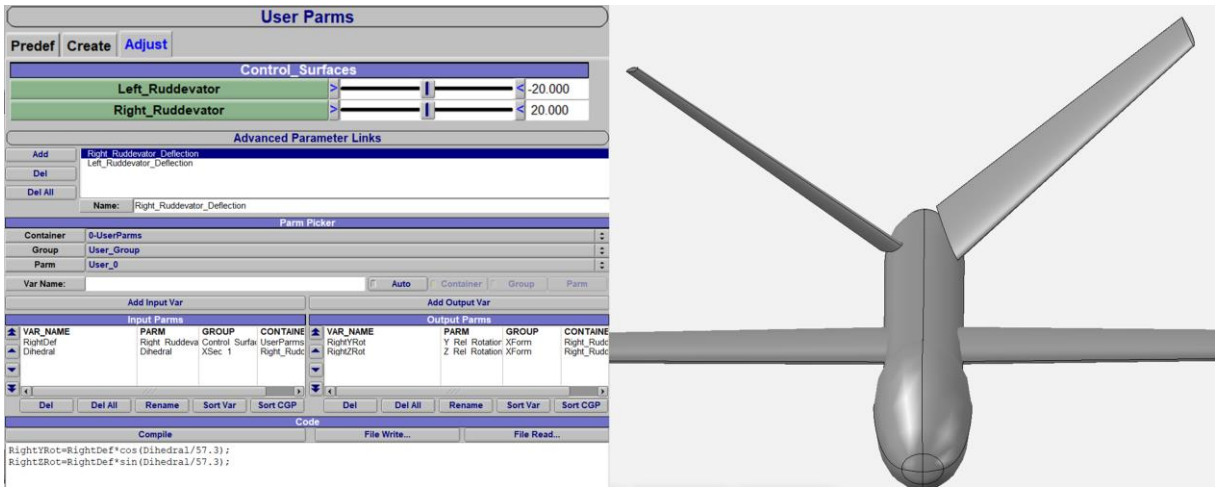

Figure 3.17 The UserParms created and an example of asymmetric rotation

As previously mentioned, the grid is identical to the one applied to the wing. The airfoil was assumed to be a standard NACA 0010.

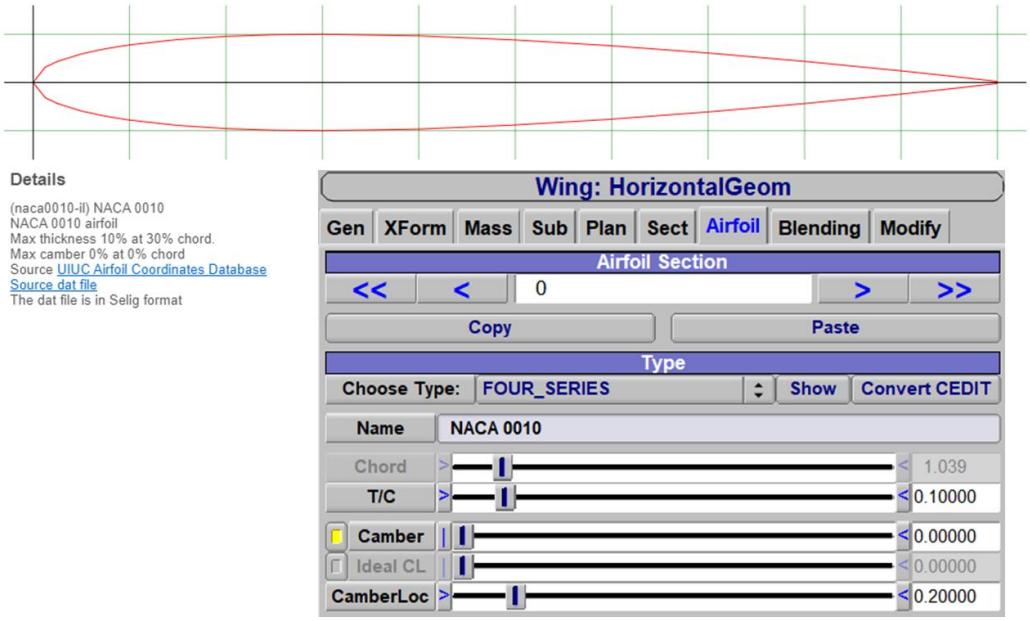

Figure 3.18 Airfoil NACA 0010 taken from www.airfoiltools.com and its parameters in OpenVSP

4. Longitudinal Aerodynamic Analysis

The aerodynamic analysis was performed using the VSPAERO tool with the Vortex Lattice Method (VLM). In this study, the reference area and lengths were automatically determined from the aircraft model. The flow conditions were set to a fixed Mach number of 0.1 and a Reynolds number of 2.5 million, reflecting the cruise speed of the Hermes. The angle of attack (α) was varied incrementally from -4° to 16° in steps of 2°, while the sideslip angle (β) was held constant at 0°. The user could choose to manually input the moment reference location or allow the software to compute these values from the model's geometry. In this analysis, the center of gravity (CG), calculated by VSPAERO, was used as the moment reference position.

With the aircraft geometry defined, the aerodynamic contributions of each component were evaluated individually. In this analysis, various configurations are addressed, with specific geometry sets selected in the VSPAERO analysis panel (Figure 4.1). All computations were performed with the wing geometry fixed, ensuring a consistent basis for evaluating the longitudinal aerodynamic characteristics of the aircraft. This approach enabled a clear assessment of the contributions of each component under the specified operating conditions.

Before going into the analysis, one last detail needs to be addressed. To illustrate the computational efficiency and speed of OpenVSP, the specifications of the laptop used for testing are provided. The device was an Asus VivoBook S15 (2018), with an 8th generation Intel Core i7 processor and 8GB of RAM. Given that this device is not exactly recent, even running a low number of wake iterations, such as three, the analysis required at least 10 minutes, occasionally leading to crashes. To overcome this, the “Fixed Wake” option was enabled in the advanced settings. This adjustment reduced the processing time to just 1 or 2 minutes, with minimal impact on the results.

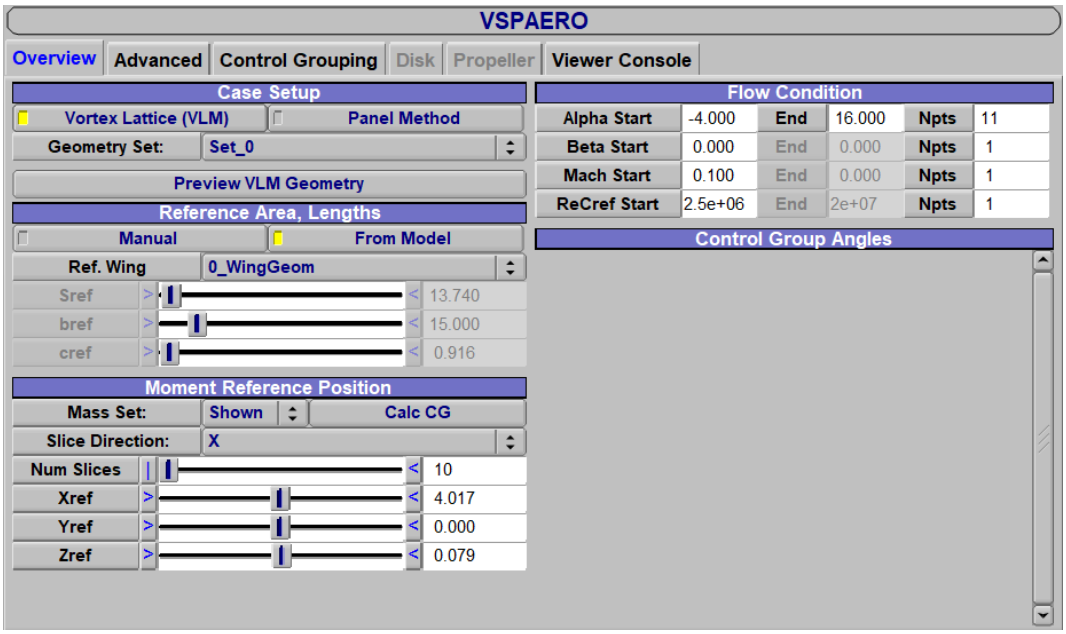

Figure 4.1 VSPAERO settings for analysis

VSPAERO generates data in text files, the files used are the .lod file, which includes the load distributions across the lifting surfaces, and the .polar file, which contains the 3D aerodynamic coefficients. The collected data were subsequently processed using Excel.

4.1 Lift coefficient curves

This paragraph focuses on the lift coefficient, specifically examining how it changes with variations in the angle of attack. Three different configurations will be considered: the Single Wing (W), the Wing with Tailplane (WT), and the Complete Aircraft.

α	C_{L_W}	$C_{L_{WT}}$	C_L
-4	0.3668	0.2645	0.2726
-2	0.5595	0.4881	0.4982
0	0.7516	0.7116	0.7237
2	0.9427	0.9347	0.9466
4	1.1328	1.1572	1.1685
6	1.3215	1.3775	1.3856
8	1.5085	1.5966	1.6070
10	1.6939	1.8120	1.8229
12	1.8771	2.0277	2.0375

14	2.0581	2.2434	2.2519
16	2.2367	2.4528	2.4602

Table 4.1 Lift coefficients

Figure 4.2 graphically reports the data present in Table 4.1.

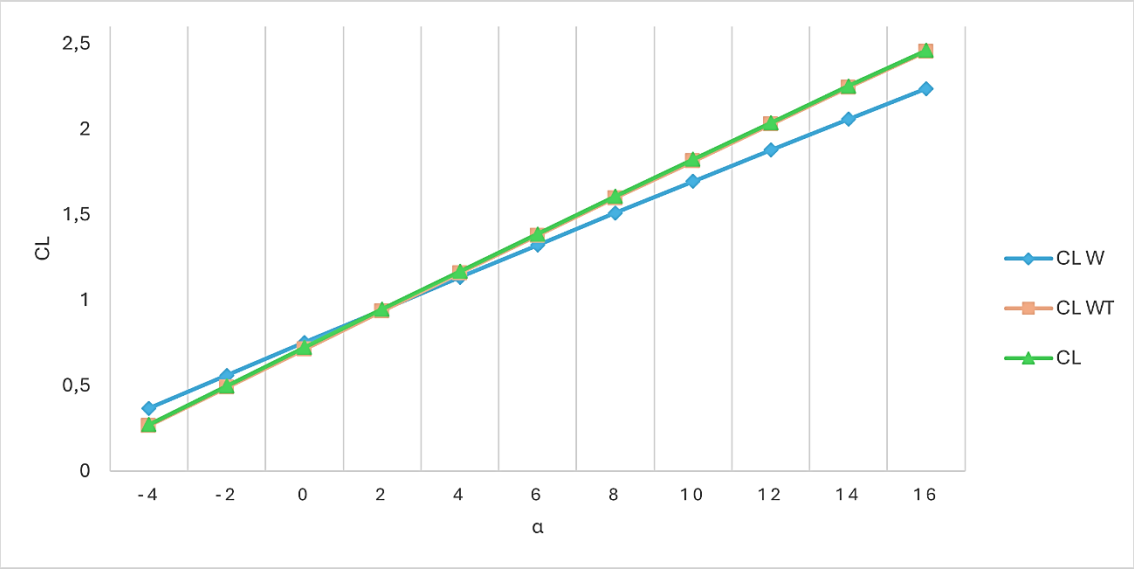

Figure 4.2 Lift coefficients curves

Since VSPAERO is unable to simulate stall conditions, the graph in Figure 4.2 shows only the linear portion of a typical lift coefficient curve. It illustrates that incorporating the tailplane increases the slope of the curve, while the addition of the fuselage has a negligible effect.

Considering the coefficients of the complete aircraft, and using the Excel slope function, we can obtain C_{L_α} which represents the overall lift curve slope of the aircraft.

$$C_{L_\alpha} = 0.1095\,\mathrm{deg}^{-1} \tag{4.1}$$

4.2 Pitching Moment coefficient curves

This paragraph will examine the pitching moment, using the same methodology applied to lift.

α	C_{M_W}	$C_{M_{WT}}$	C_M
-4	-0.1609	0.2574	0.0241
-2	-0.1259	0.2814	-0.0875
0	-0.0902	0.3045	-0.2027

2	-0.0542	0.3267	-0.3210
4	-0.0178	0.3470	-0.4339
6	0.0187	0.3688	-0.5316
8	0.0551	0.3872	-0.6521
10	0.0914	0.4125	-0.7578
12	0.1273	0.4281	-0.8676
14	0.1628	0.4348	-0.9856
16	0.1976	0.4506	-1.0893

Table 4.2 Pitching moment coefficients

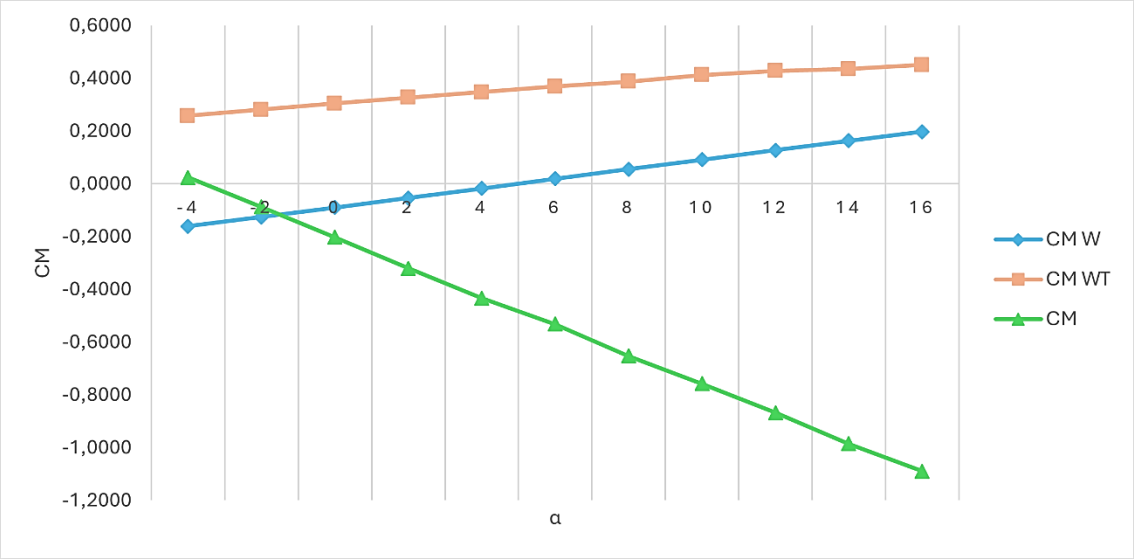

Figure 4.3 Pitching moment coefficients curves

Table 4.2 and Figure 4.3 reveals that both the isolated wing configuration and the wing and tail configuration exhibit unstable behavior. It is with the addition of the fuselage that the UAV reaches longitudinal stability, as indicated by a negative slope in the C_M curve at the equilibrium point.

By using Excel's slope function again for the complete aircraft configuration, we obtain C_{M_α}, which represents the slope of the total aircraft's pitching moment curve. As expected, this value is negative.

$$C_{M_\alpha} = -0.0556\,\mathrm{deg}^{-1} \tag{4.2}$$

4.2.1 Neutral Point and Static Margin

A suitable formula for calculating C_{M_α} is:

$$C_{M_\alpha} = C_{L_\alpha}(\overline{X}_G - \overline{X}_N) \tag{4.3}$$

Where $\overline{X}_G$ is the normalized position of the center of gravity, and $\overline{X}_N$ is the normalized position of the neutral point. The distance between them is crucial as it indicates the static margin.

$$SM = \overline{X}_G - \overline{X}_N \tag{4.4}$$

The Table 4.3 presents the obtained values.

$\mathbf{C_{L_\alpha}}$	0.1095 deg^{-1}
$\mathbf{C_{M_\alpha}}$	-0.0556 deg^{-1}
$\mathbf{\overline{X}_G}$	4.017
$\mathbf{\overline{X}_N}$	4.525
SM	-0.508

Table 4.3 Values of important elements for static stability

It is evident that the center of gravity is positioned ahead of the neutral point, further confirming the aircraft's static stability.

The correctness of the value of $\overline{X}_N$ is evaluated by examining the change in the moment when the reference position in manually varied between $\overline{X}_G$ and $\overline{X}_N$. Two intermediate points are selected for this purpose: $\overline{X}_1 = 4.246$ and $\overline{X}_2 = 4.385$.

$\boldsymbol{\alpha}$	$\mathbf{C_M}$	$\mathbf{C_{M_{X1}}}$	$\mathbf{C_{M_{X2}}}$	$\mathbf{C_{M_{XN}}}$
-4	0.0241	0.0924	0.1338	0.1754
-2	-0.0875	0.0373	0.1130	0.1891
0	-0.2027	-0.0209	0.0893	0.2003
2	-0.3210	-0.0826	0.0618	0.2073
4	-0.4339	-0.1395	0.0389	0.2186
6	-0.5316	-0.1825	0.0290	0.2420

8	-0.6521	-0.2477	-0.0026	0.2442
10	-0.7578	-0.2999	-0.0224	0.2570
12	-0.8676	-0.3572	-0.0478	0.2638
14	-0.9856	-0.4234	-0.0827	0.2605
16	-1.0893	-0.4776	-0.1070	0.2664

Table 4.4 Pitching moment coefficients at various reference points

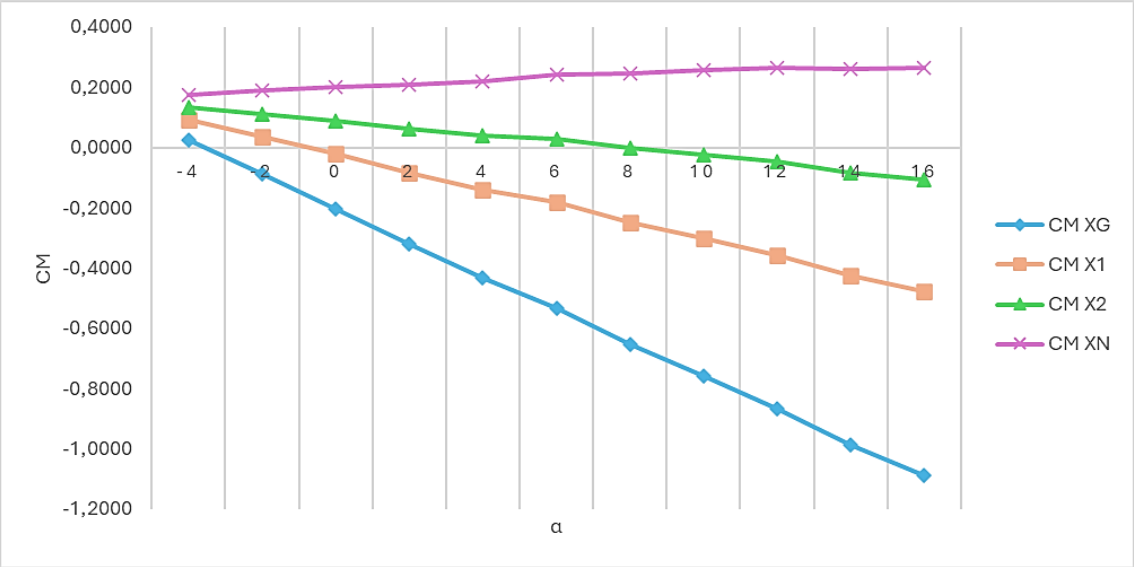

Figure 4.4 Pitching moment coefficients curves at various reference points

For a complete analysis, the slopes of each plotted value are also reported in Table 4.5.

$\mathbf{C_{M_\alpha}(X_G)}$	-0.0556 deg^{-1}
$\mathbf{C_{M_\alpha}(X_1)}$	-0.0284 deg^{-1}
$\mathbf{C_{M_\alpha}(X_2)}$	-0.0119 deg^{-1}
$\mathbf{C_{M_\alpha}(X_N)}$	0.0048 deg^{-1}

Table 4.5 Slopes of pitching moments coefficients at various reference points

It can be observed that as the reference position approaches the neutral point, the slope decreases, according with the theoretical expectation. The calculated value of the neutral point is not perfectly exact, as the slope should ideally be zero; however, it represents a reasonably accurate estimate given the simplicity of the method used to obtain it.

4.3 Drag coefficient and Aerodynamic Efficiency curves

α	C_{D_W}	$C_{D_{WT}}$	C_D
-4	0.0119	0.0156	0.0158
-2	0.0167	0.0194	0.0198
0	0.0234	0.0258	0.0263
2	0.0319	0.0348	0.0355
4	0.0423	0.0463	0.0470
6	0.0543	0.0604	0.0606
8	0.0680	0.0769	0.0769
10	0.0834	0.0956	0.0952
12	0.1002	0.1169	0.1156
14	0.1184	0.1406	0.1385
16	0.1380	0.1662	0.1629

Table 4.6 Drag coefficients

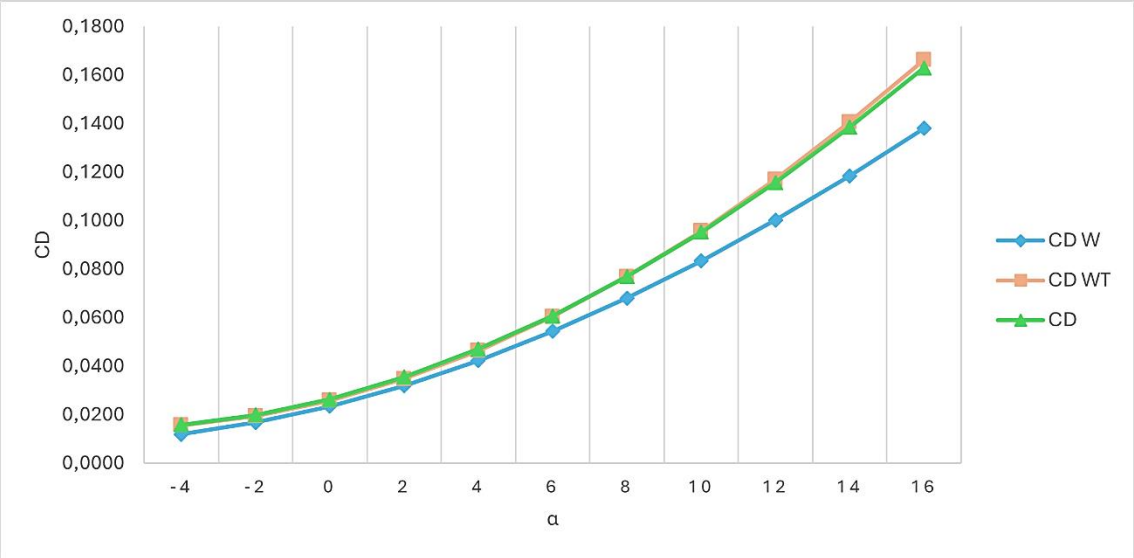

Figure 4.5 Drag coefficients curves

From Figure 4.5 it is clear how minimal is the impact of the fuselage on drag, and this is attributed to how VSPAERO computes drag. Specifically, the tool calculates only induced drag, meaning that only the lifting surfaces contribute significantly to the drag curve.

α	E_W	E_{WT}	E
-4	30.72	16.99	17.30
-2	33.43	25.20	25.21
0	32.09	27.61	27.50
2	29.51	26.88	26.67
4	26.80	24.97	24.85
6	24.33	22.81	22.87
8	22.17	20.76	20.90
10	20.32	18.95	19.16
12	18.74	17.35	17.62
14	17.38	15.95	16.25
16	16.21	14.76	15.10

Table 4.7 Aerodynamic efficiency

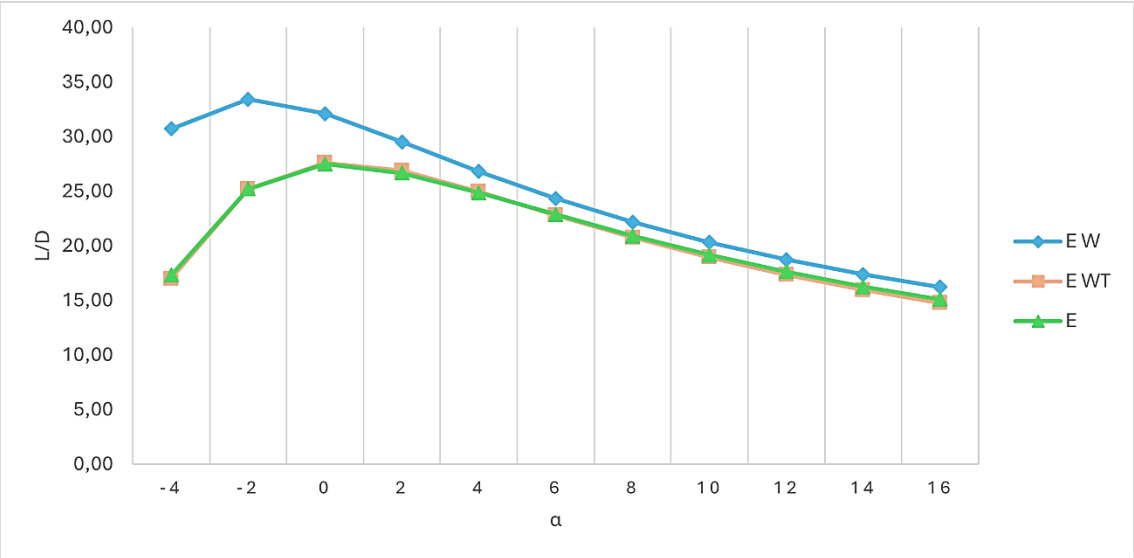

Figure 4.6 Aerodynamic efficiency curves

4.4 Impact of ruddervators on longitudinal aerodynamics

The next objective of the analysis is to illustrate the effects of ruddervators deflection on the previously presented aerodynamic curves. Symmetrical deflections were applied at angles of 5°, -5°, -10°, -15°, and -20°. The outcomes, derived from the inputs entered in the UserParms, are shown through summary tables and graphs.

4.4.1 Lift

α	$C_{L,\delta_e=5°}$	$C_{L,\delta_e=0°}$	$C_{L,\delta_e=-5°}$	$C_{L,\delta_e=-10°}$	$C_{L,\delta_e=-15°}$	$C_{L,\delta_e=-20°}$
-4	0.3803	0.2726	0.1830	0.0915	0.0074	-0.0675
-2	0.6018	0.4982	0.4014	0.3083	0.2221	0.1454
0	0.8227	0.7237	0.6200	0.5253	0.4371	0.3570
2	1.0421	0.9466	0.8374	0.7410	0.6508	0.5683
4	1.2603	1.1685	1.0543	0.9561	0.8639	0.7793
6	1.4749	1.3856	1.2695	1.1702	1.0760	0.9890
8	1.6896	1.6070	1.4829	1.3821	1.2862	1.1972
10	1.8991	1.8229	1.6929	1.5912	1.4960	1.4039
12	2.1087	2.0375	1.9018	1.7997	1.7010	1.6085
14	2.3142	2.2519	2.1080	2.0055	1.9056	1.8111
16	2.5162	2.4602	2.3102	2.2083	2.1085	2.0135

Table 4.8 Lift coefficients as δ_e varies

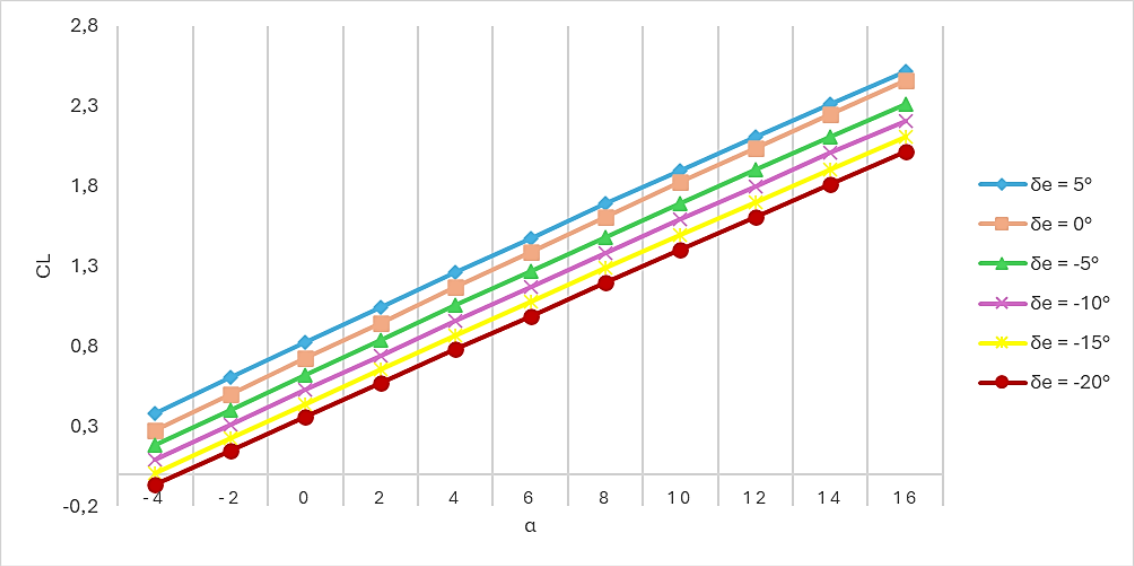

Figure 4.7 C_L vs α as δ_e varies

Negative and symmetric deflections of the ruddervators result in increased downforce on the tailplane, leading to lower overall lift coefficients for the aircraft, as clearly illustrated in the Figure 4.7.

Using the formula:

$$C_{L_{\delta e}} = \frac{C_{L_0}(\delta) - C_{L_0}(\delta=0)}{\delta} \tag{4.5}$$

We can calculate the lift control derivative for the elevators.

$$C_{L_{\delta e}} = 0.0188\,\mathrm{deg}^{-1} \tag{4.6}$$

The positive value indicates that, as with negative deflections, the lift decreases.

4.4.2 Pitching moment

α	$C_{M,\delta_e=5°}$	$C_{M,\delta_e=0°}$	$C_{M,\delta_e=-5°}$	$C_{M,\delta_e=-10°}$	$C_{M,\delta_e=-15°}$	$C_{M,\delta_e=-20°}$
-4	-0.2464	0.0924	0.3811	0.6782	0.9561	-0.0722
-2	-0.2938	0.0373	0.3471	0.6505	0.9356	1.1963
0	-0.3429	-0.0209	0.3110	0.6203	0.9121	1.1803
2	-0.3955	-0.0826	0.2686	0.5839	0.8824	1.1570
4	-0.4443	-0.1395	0.2301	0.5512	0.8569	1.1377
6	-0.4869	-0.1825	0.1935	0.5197	0.8312	1.1191
8	-0.5378	-0.2477	0.1537	0.4872	0.8038	1.0984
10	-0.5787	-0.2999	0.1212	0.4612	0.7768	1.0797
12	-0.6283	-0.3572	0.0823	0.4245	0.7517	1.0577
14	-0.6724	-0.4234	0.0431	0.3890	0.7195	1.0333
16	-0.7110	-0.4776	0.0085	0.3554	0.6907	1.0068

Table 4.9 Pitching moment coefficients as δ_e varies

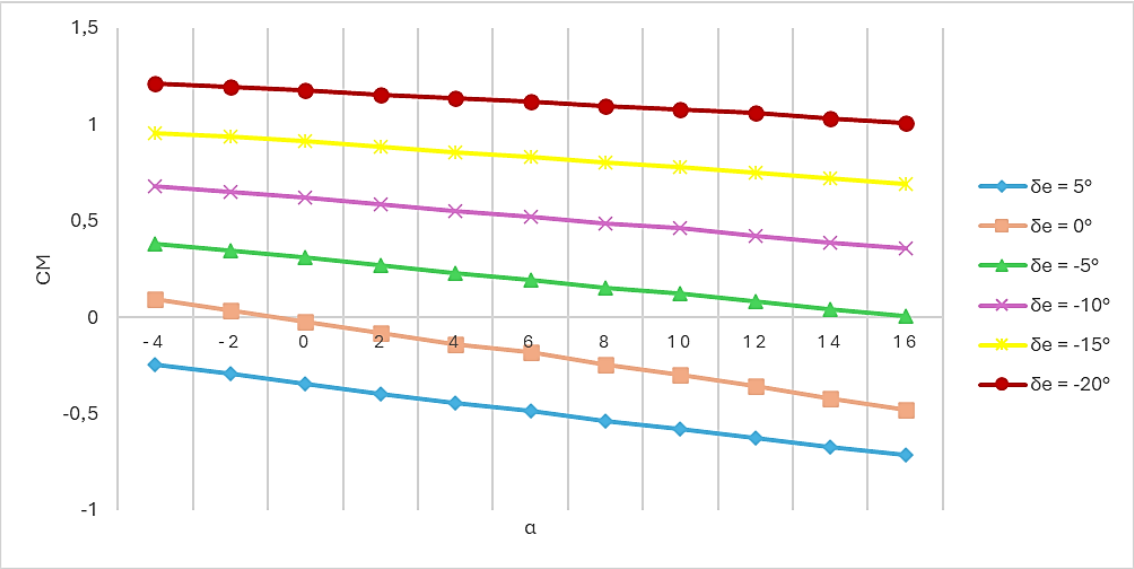

Figure 4.8 C_M vs α as δ_e varies

As before, we can calculate the control derivative:

$$C_{M_{\delta e}} = -0.0613\,\mathrm{deg}^{-1} \tag{4.7}$$

The negative sign indicates that negative elevator deflections increase C_M, as shown in Figure 4.8.

4.4.3 Drag

α	$C_{D,\delta_e=5°}$	$C_{D,\delta_e=0°}$	$C_{D,\delta_e=-5°}$	$C_{D,\delta_e=-10°}$	$C_{D,\delta_e=-15°}$	$C_{D,\delta_e=-20°}$
-4	0.0154	0.0158	0.0223	0.0338	0.0499	0.0696
-2	0.0214	0.0198	0.0244	0.0341	0.0487	0.0673
0	0.0299	0.0263	0.0288	0.0368	0.0499	0.0671
2	0.0409	0.0355	0.0357	0.0418	0.0532	0.0691
4	0.0542	0.0470	0.0448	0.0490	0.0587	0.0732
6	0.0696	0.0606	0.0562	0.0584	0.0662	0.0791
8	0.0875	0.0769	0.0697	0.0699	0.0761	0.0873
10	0.1069	0.0952	0.0851	0.0833	0.0870	0.0969
12	0.1290	0.1156	0.1025	0.0985	0.1005	0.1082
14	0.1525	0.1385	0.1218	0.1158	0.1156	0.1214
16	0.1777	0.1629	0.1428	1.1344	0.1323	0.1363

Table 4.10 Drag coefficients as δ_e varies

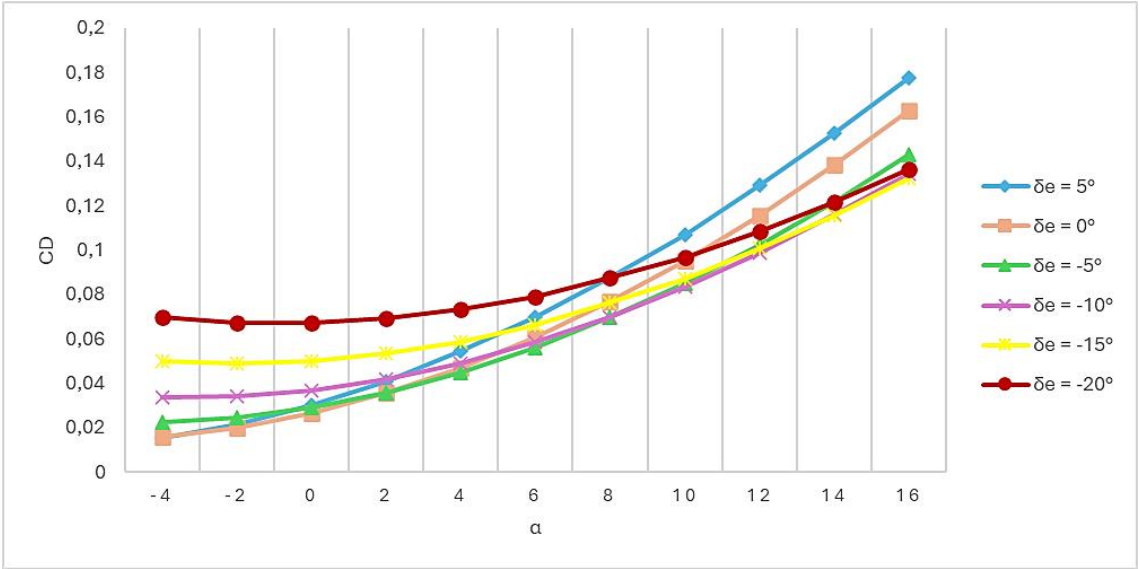

Figure 4.9 C_D vs α as δ_e varies

5. Lateral-Directional Aerodynamic Analysis

The conditions for conducting the lateral and directional aerodynamic analysis are similar to those applied in the longitudinal analysis. The Mach and Reynolds numbers are kept constant, maintaining the values used in the previous analysis. However, in this case, the angle of attack α is fixed at 0°, while the sideslip angle β is varied from -4° to 20° in steps of 2°, with the XZ symmetry disabled. Another important difference is the placement of the center of gravity. As indicated in Table 4.4 and Figure 4.4, positioning the CG at $\overline{X}_1$ results in the system being nearly trimmed at α = 0°, making this a practical value to use. The coefficients discussed in this analysis are rolling moment coefficient C_R, yawing moment coefficient C_N, and sideforce coefficient C_Y.

β	C_R	C_N	C_Y
-4	$-2.86\text{x}10^{-3}$	$4.11\text{x}10^{-3}$	$2.79\text{x}10^{-2}$
-2	$-1.32\text{x}10^{-3}$	$3.32\text{x}10^{-3}$	$1.43\text{x}10^{-2}$
0	$1.01\text{x}10^{-5}$	$-2.30\text{x}10^{-5}$	$9.38\text{x}10^{-5}$
2	$1.35\text{x}10^{-3}$	$-3.41\text{x}10^{-3}$	$-1.44\text{x}10^{-2}$
4	$2.87\text{x}10^{-3}$	$-4.16\text{x}10^{-3}$	$-2.80\text{x}10^{-2}$
6	$4.17\text{x}10^{-3}$	$-7.49\text{x}10^{-3}$	$-4.19\text{x}10^{-2}$
8	$5.67\text{x}10^{-3}$	$-8.85\text{x}10^{-3}$	$-5.57\text{x}10^{-2}$
10	$7.07\text{x}10^{-3}$	$-1.08\text{x}10^{-2}$	$-6.90\text{x}10^{-2}$
12	$8.45\text{x}10^{-3}$	$-9.86\text{x}10^{-3}$	$-8.18\text{x}10^{-2}$
14	$9.56\text{x}10^{-3}$	$-1.13\text{x}10^{-2}$	$-9.36\text{x}10^{-2}$
16	$1.06\text{x}10^{-2}$	$-1.60\text{x}10^{-2}$	$-1.06\text{x}10^{-1}$
18	$1.24\text{x}10^{-2}$	$-1.67\text{x}10^{-2}$	$-1.17\text{x}10^{-1}$
20	$1.34\text{x}10^{-2}$	$-1.96\text{x}10^{-2}$	$-1.31\text{x}10^{-1}$

Table 5.1 Rolling moment, yawing moment and sideforce coefficients with various sideslip angles

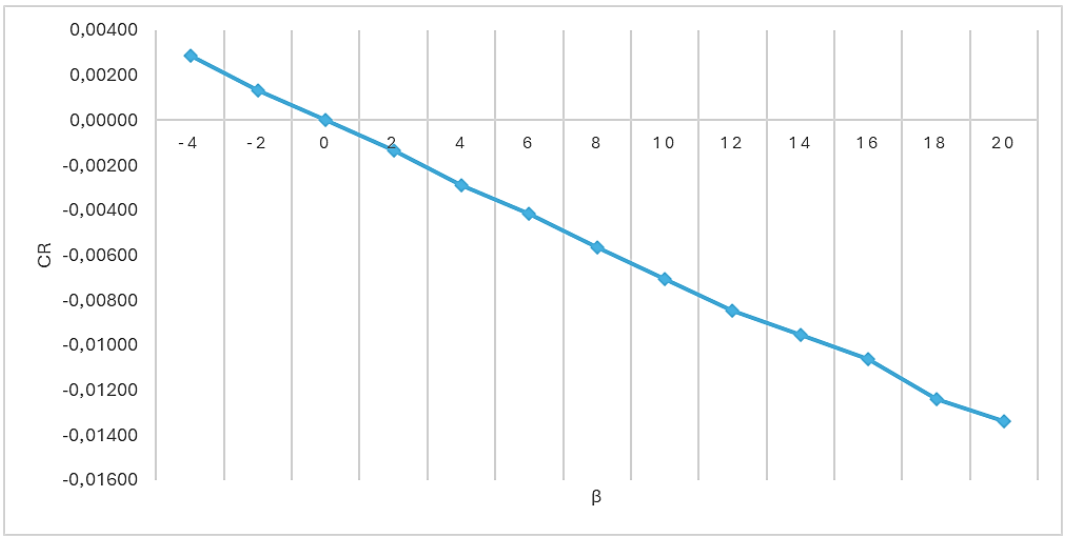

Figure 5.1 C_R vs β

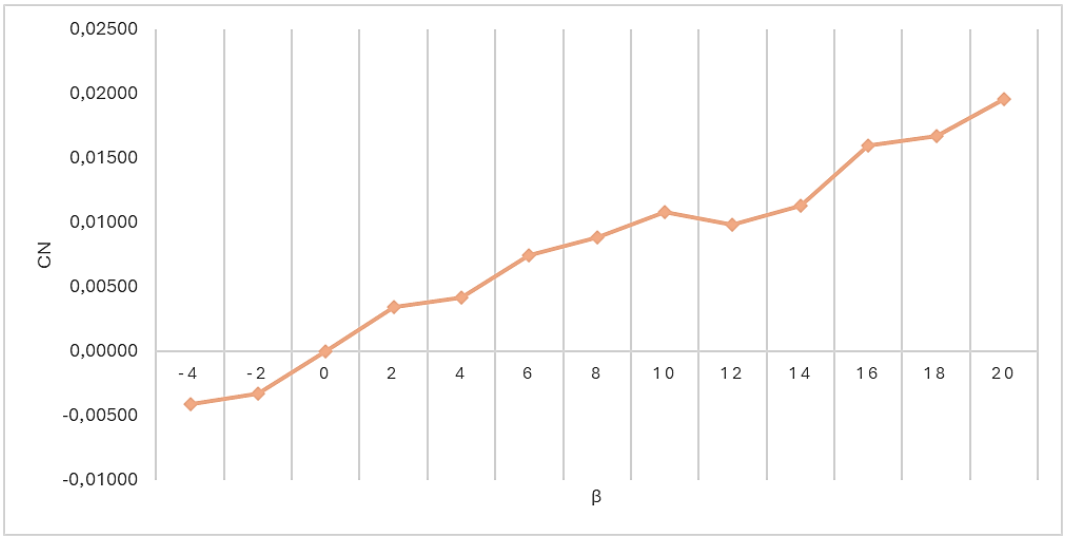

Figure 5.2 C_N vs β

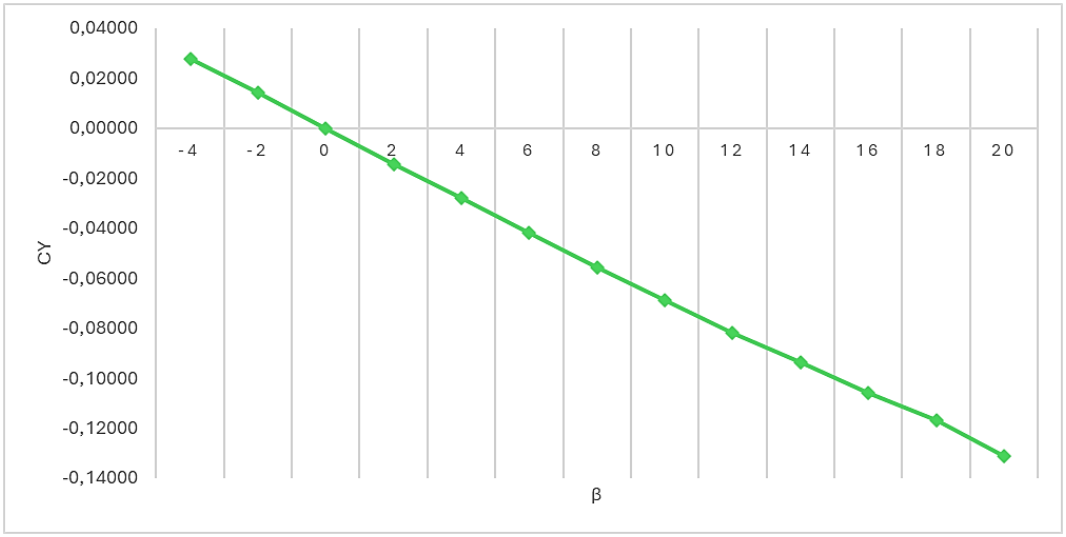

Figure 5.3 C_Y vs β

The graphs are presented in the body reference frame (BRF). It is important to note that VSPAERO calculates momentum coefficients in a constructive reference frame, where the X and Z axes are inverted relative to the BRF. To account for this, the signs of the output moments were simply inverted.

It is evident that the symmetry of the aircraft results in coefficients that are practically zero at β = 0°. The slopes presented in Figure 5.1 and Figure 5.2 (negative for C_R and positive for C_N) demonstrate that the UAV exhibits both lateral and directional stability.

6. Conclusions

Table 6.1 summarizes the main stability and control derivatives found in the analysis.

$\mathbf{C_{L_\alpha}}$	0.1095 deg^{-1}
$\mathbf{C_{M_\alpha}(X_1)}$	-0.0284 deg^{-1}
$\mathbf{C_{M_{x\beta}}}$	-0.0007 deg^{-1}
$\mathbf{C_{M_{z\beta}}}$	0.0009 deg^{-1}
$\mathbf{C_{L_{\delta e}}}$	0.0188 deg^{-1}
$\mathbf{C_{M_{\delta e}}}$	-0.0613 deg^{-1}

Table 6.1 Stability and control derivatives

This thesis has demonstrated how using OpenVSP and VSPAERO provide an efficient solution for conducting preliminary aerodynamic analyses of aircraft designs. Although VSPAERO is not designed to evaluate all aerodynamic behaviors with complete accuracy, its main advantage lies in providing quick and simple results without the need for extensive CFD simulations or wind tunnel tests. This capability significantly expedites the early stages of the design process. However, it is important to acknowledge its limitations, particularly when managing more complex models, where the simplified flow assumptions may lead to less accurate outcomes.

Bibliography

[1] Advanced UAV aerodynamics, Flight stability and control, Pascual Marqués, Andrea Da Ronch John Wiley & Sons, Apr 27, 2017.

[2] Software Testing: VSPAERO, Floris Mariën, Prof. Dr.-Ing. Dieter Scholtz, 16/07/2021.

[3] OpenVSP website: http://openvsp.org

[4] Airfoil Tools website: http://airfoiltools.com

[5] OpenVSP ground school website: https://vspu.larc.nasa.gov

[6] Avions Legendaires, Elbit Hermes 900.